


Article

# A Remarkable Photocatalyst Filter for Indoor Air Treatment

Vijayarohini Parasuraman <sup>1,2,†</sup>, Parasuraman Perumalswamy Sekar <sup>2,3,†</sup>, Hojae Lee <sup>4</sup> , Mahshab Sheraz <sup>2,3</sup>,  
Woo Ram Lee <sup>5,\*</sup>, Tae Young Park <sup>6</sup> and Seungdo Kim <sup>1,2,3,7,\*</sup>

<sup>1</sup> Research Center for Climate Change and Energy (RCCCE), Hallym University, Chuncheon 24252, Republic of Korea

<sup>2</sup> Nano-InnoTek Corporation, 123, Digital-ro 26-gil, Guro-gu, Seoul 08390, Republic of Korea

<sup>3</sup> Department of Environmental Sciences and Biotechnology, Hallym University, Chuncheon 24252, Republic of Korea

<sup>4</sup> Department of Chemistry, Hallym University, Chuncheon 24252, Republic of Korea

<sup>5</sup> Department of Chemistry, School of Future Convergence, Hallym University, Chuncheon 24252, Republic of Korea

<sup>6</sup> Department of Industrial Co-Operation, Konkuk University, Seoul 08390, Republic of Korea

<sup>7</sup> Environment Strategy Development Institute (ESDI), Chuncheon 24252, Republic of Korea

\* Correspondence: alchemist@hallym.ac.kr (W.R.L.); sdkim@hallym.ac.kr (S.K.)

† These authors contributed equally to this work.

**Abstract:** A crucial environmental public health risk is air pollution caused by organic contaminants, bio-aerosols, and fine particulate matter (PM<sub>2.5-10</sub>). A multi-purpose photocatalyst filter with photocatalytic nitrogen-doped titanium dioxide (PNT) incorporated into non-woven polymer fibers (NWPF) with wide applications is focused on in detail in this work. Loading of PNT on NWPF is carried out by the simple dip coating method. Para-xylene is selected as the target pollutant for the removal of organic contaminants. Higher removal efficiency of *p*-xylene (94.2%) is achieved under fluorescent daylight. The filtration efficiency of PNT is also evaluated to capture PM<sub>2.5-10</sub>, which is increased with higher loading content of PNT. At a high air flow rate, the filtration efficiency of the photocatalyst PNT/NWPF is 97.33%, whereas the efficiency of the pristine NWPF is 91.1%. Moreover, the PNT/NWPF filter exhibits excellent antibacterial activity (99.9%) under visible light irradiation, but the pristine NWPF filter has negligible destruction effects on pathogens. These results clearly indicate that a PNT-coated NWPF filter would be an outstanding multi-purpose material for indoor air purification systems.

**Keywords:** PNT nanospheres; PM<sub>2.5-10</sub>; dust capture; VOC removal; *p*-xylene; pathogen; *E. coli*; disinfection



**Citation:** Parasuraman, V.; Sekar, P.P.; Lee, H.; Sheraz, M.; Lee, W.R.; Park, T.Y.; Kim, S. A Remarkable Photocatalyst Filter for Indoor Air Treatment. *Catalysts* **2022**, *12*, 1433. <https://doi.org/10.3390/catal12111433>

Academic Editors: Kyubock Lee and Min-Jae Kim

Received: 14 October 2022

Accepted: 11 November 2022

Published: 14 November 2022

**Publisher's Note:** MDPI stays neutral with regard to jurisdictional claims in published maps and institutional affiliations.



**Copyright:** © 2022 by the authors. Licensee MDPI, Basel, Switzerland. This article is an open access article distributed under the terms and conditions of the Creative Commons Attribution (CC BY) license (<https://creativecommons.org/licenses/by/4.0/>).

## 1. Introduction

The increased personal time (over 80%) consumed in indoor environments such as residential buildings, the workplace, car, and shopping plazas has made indoor air quality (IAQ) a significant global issue [1–3]. Indoor air quality (IAQ) is considered even worse than that of outdoor air because toxic by-products are produced due to the combustion of fuel from industry and are continuously emitted from construction materials and consumer products [4]. Particulates, such as nitrogen oxides (NO<sub>x</sub>), carcinogenic carbon oxides (CO and CO<sub>2</sub>), and volatile organic compounds (VOCs), are the main pollutants detected from such sources [5]. Many VOCs are toxic, which leads to cancer, mutagenesis, and teratogenic effects. Sick building syndrome (SBS), a chronic illness characterized by headache, dizziness, dry skin, irritation (eye, nose, and throat), a dry cough, fatigue, and asthma attacks, may be the result of long-standing exposure to (VOCs) [6–8].

Particularly in South Korea, around 70% of the emissions are from the industrial complex sources. A survey of hazardous pollutant emissions in this specific geometrical zone was surveyed from 2007 to 2016 [9]. As of 2016, a total of 57,247,000 kg of toxic chemical

compounds were discharged from 3732 places of industry across the country, compared with 47,688,000 kg in 2007. There was a 1.24-fold increase in business establishments and a 1.20-fold increase in emissions observed during the same period. Moreover, the majority of the harmful chemical discharges are released into the atmosphere. The major pollutants emitted are xylene and toluene, followed by ethyl acetate, ethyl benzene, and methyl ethyl ketone [10]. In the Ulsan, Samho, Mipo, Jukdo, and Mipo regions, xylene displayed the largest emissions, followed by ethyl benzene and toluene [11]. Further, in these zones, the effect of these emissions affects the air quality present in both outdoor and indoor environments such as homes, schools, public buildings, and health care centers.

The pollutant xylene is majorly emitted from the industrial zones and used in the preparation of paint thinners or as solvent in the manufacturing of automobiles, plastic, and rubber products, which easily evaporate into the atmosphere [12,13]. As a result of exposure to xylene, one can experience irritation to the eyes, nose, and throat as well as neurological effects. Toluene is also a toxic substance that can also be quickly absorbed through lungs when inhaled, mainly because it also has a neurotoxic effect. These pollutants are associated with the cause of allergens and development of various allergic diseases.

In order to minimize exposure to various contaminants, several strategies have to be taken. Despite the highly polluted air which has been worsened by human activities, air filtration has received much interest in preserving the desired environment [14]. The contaminants in the air include fine particulate matter (PM<sub>2.5</sub>), toxic gaseous pollutants, and harmful pathogens. So, it is a challenge to eliminate all sources of pollution in the most effective and convenient way. In order to remove all these mentioned elements, individual air filters (removal of VOC, dust, pathogens) for each specific purpose have been widely used [15,16]. Photocatalysts are commonly utilized to remove toxic chemical compounds effectively [17–19]. Metal oxides, such as titanium di-oxide (TiO<sub>2</sub>), immobilized on solid substrates are activated under ultraviolet light, producing ROS species such as hydroxyl and superoxide anion radicals that react with the chemicals and decompose them into carbon dioxide and water [20]. However, using solid substrates is ineffective because contaminants adsorbed on the solid substrates accumulate over time, causing the photocatalyst poisoning to reduce the filter's lifetime. The use of UV lights is also challenging because of high-energy consumption and maintenance for its use [21]. TiO<sub>2</sub> does not absorb visible light (>50% in the sunlight) because of its wide bandgap [22].

For this purpose, TiO<sub>2</sub> is doped with non-metals such as nitrogen, carbon, sulfur, or with metals such as copper, silver, manganese, or zinc, which extends the absorption of light in the visible light region [23–26]. Photocatalytic nitrogen-doped titanium dioxide (PNT), especially, has been extensively investigated in various research works [27–30]. However, the utilization of PNT in air filters has not been studied so far. In this study, PNT-coated air filters were fabricated by simple coating technology. The capture of fine dust particles (PM<sub>2.5–10</sub>), destruction of xylene, toxic volatile organic compound, and disinfection of pathogen *E. coli* is evaluated using multi-purpose PNT-coated air filter which is active under fluorescent light.

## 2. Results and Discussion

### 2.1. Characterization of PNT

Diffuse reflectance spectra of TiO<sub>2</sub> (P25) and nitrogen-doped TiO<sub>2</sub> samples are shown in Figure 1a. Nitrogen doping extends the light absorption with two characteristic absorption edges with a notable red-shift in the visible region around 400 to 800 nm. The first is due to electron shift from the valence band to the conduction band, while the second comes from new energy levels in the forbidden band of P25 formed by N-doping. Moreover, the Kubelka–Munk function is applied to compute the band gap of the samples [31]. Data on  $[F(R)*E]^{1/2}$  versus photon energy (hν) is shown in Figure 1b. The values of band gap energy are found to be 3.22 eV and 2.82 eV for P25 TiO<sub>2</sub> and PNT, respectively. From this result, it is clearly confirmed that PNT has high photocatalytic activity under visible light. The XPS spectra of PNT nanoparticles are shown in Figure 1c–e for N1s, O1s, and Ti2p energy

levels, respectively. In Figure 1c, it has been clearly demonstrated that the core level of the Nitrogen 1s peak in PNT occurred at 398.2 eV since the anionic nitrogen present in the O-Ti-N linkage [32]. It is expected that either simple chemisorbed nitrogen or TiN appears at  $\leq 397.5$  eV, and NO or NO<sub>2</sub> species appear perhaps at 400 eV or even higher. On the contrary, the N1s peak at 398.2 supports the hypothesis that nitrogen is associated into the TiO<sub>2</sub> lattice as the N-Ti-O linkage indicates substitutional doping [33]. Figure 1d represents the O1s spectra of PNT with a peak at 530.28 eV that indicates a Ti-O bond [34]. The PNT sample however shows a broadening on the higher BE side at 531.5 eV. There might be possibilities that PNT has a divergent type of oxygen owing to its characteristic covalent nature. This is such that both oxygen and nitrogen elements are accessible in TiO<sub>2</sub> from the same lattice units. The Ti2p spectrum of the PNT sample displayed two distinct energy levels at 458.05 and 463.74 eV, which confirms the Ti2p<sub>3/2</sub> and Ti2p<sub>1/2</sub>, which supports the presence of the Ti<sup>4+</sup> species as depicted in Figure 1e [35]. Thus, a small shift in the binding energy is observed for PNT compared with P25 [36] due to the interaction between nitrogen and titanium. These results are further supported by FT-IR spectroscopy. Figure 1f presents the FT-IR spectrum of P25 and PNT photocatalysts. The corresponding TiO<sub>2</sub> bands at 450–800 cm<sup>-1</sup>, 1610 cm<sup>-1</sup>, and 3250–3600 cm<sup>-1</sup> are present in both P25 and PNT. A broad band at 450–800 cm<sup>-1</sup> is attributed to O-Ti-O vibrations, while broad bands at 1610 cm<sup>-1</sup> and 3250–3600 cm<sup>-1</sup> in PNT are caused due to the adsorption of water and the vibration of the -OH stretching and bending group. As a result of the enlargement of prominent bands of hydroxyl groups caused by the nitrogen incorporation onto TiO<sub>2</sub>, the catalyst has the capacity to generate more highly reactive hydroxyl radicals during photocatalysis, enhancing their performance. TiO<sub>2</sub> doping with nitrogen showed additional vibration bands at 1232 cm<sup>-1</sup> and 1160 cm<sup>-1</sup> corresponding to Ti-N vibrations.

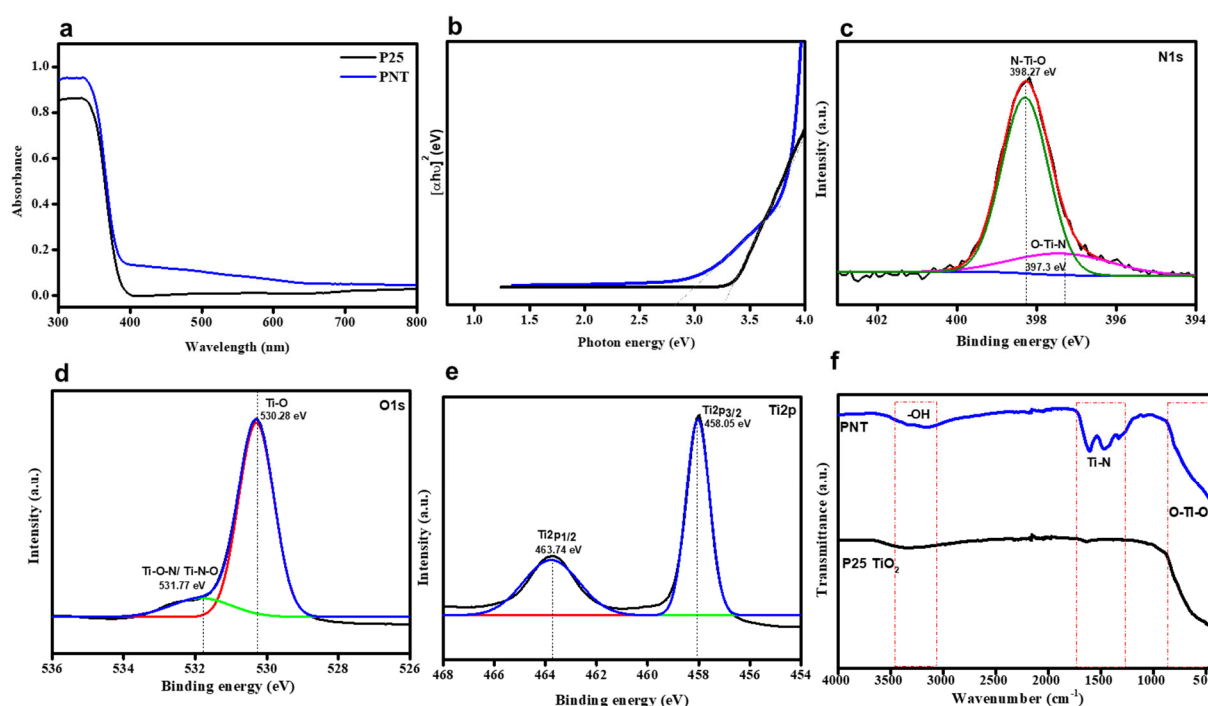


**Figure 1.** (a) UV-VIS diffuse reflectance spectra of P25 and PNT samples. (b) Band gap value of P25 and PNT samples. (c) XPS spectra of N1s, (d) XPS spectra of O1s, (e) XPS spectra of Ti2p, (f) FT-IR spectra of P25 TiO<sub>2</sub> and PNT.

## 2.2. Morphology and Photoluminescence Spectra of PNT

The surface morphology of the PNT nanoparticles is photographed by scanning electron microscopy (SEM) in Figure 2a; the spherical-shaped nanoparticles are clearly seen. Figure 2b depicts the HR-TEM image of the synthesized PNT nanoparticles. A lattice

fringe of 0.350 nm and 0.240 nm was observed because of the anatase lattice plane (101) of TiO<sub>2</sub> nanoparticles and 0.320 nm because of the rutile lattice plane (110) of pure TiO<sub>2</sub> (Figure 2c,d). Photoluminescence (PL) spectra is an excellent tool to study how well charge carriers trap, migrate, and transfer because the PL emissions result from the recombination of free carriers [37]. TiO<sub>2</sub> absorbs incident photons with energy equal to or higher than the band gap energy, producing photoinduced charge carriers (e<sup>-</sup> h<sup>+</sup>). Further, PL emission spectra are produced by the recombination of electrons and holes. Thus, a low PL intensity specifies less charge recombination. The PL emission spectra for TiO<sub>2</sub> and PNT are shown in Figure 2e. The faster recombination of photoinduced charge carriers in TiO<sub>2</sub> resulted in a higher PL intensity. When nitrogen (N) is introduced to TiO<sub>2</sub>, the intensity is lowered. Hence, the PL results confirm that N states serve as a hole reservoir for inducing excitations and improving electron-hole separation [38].

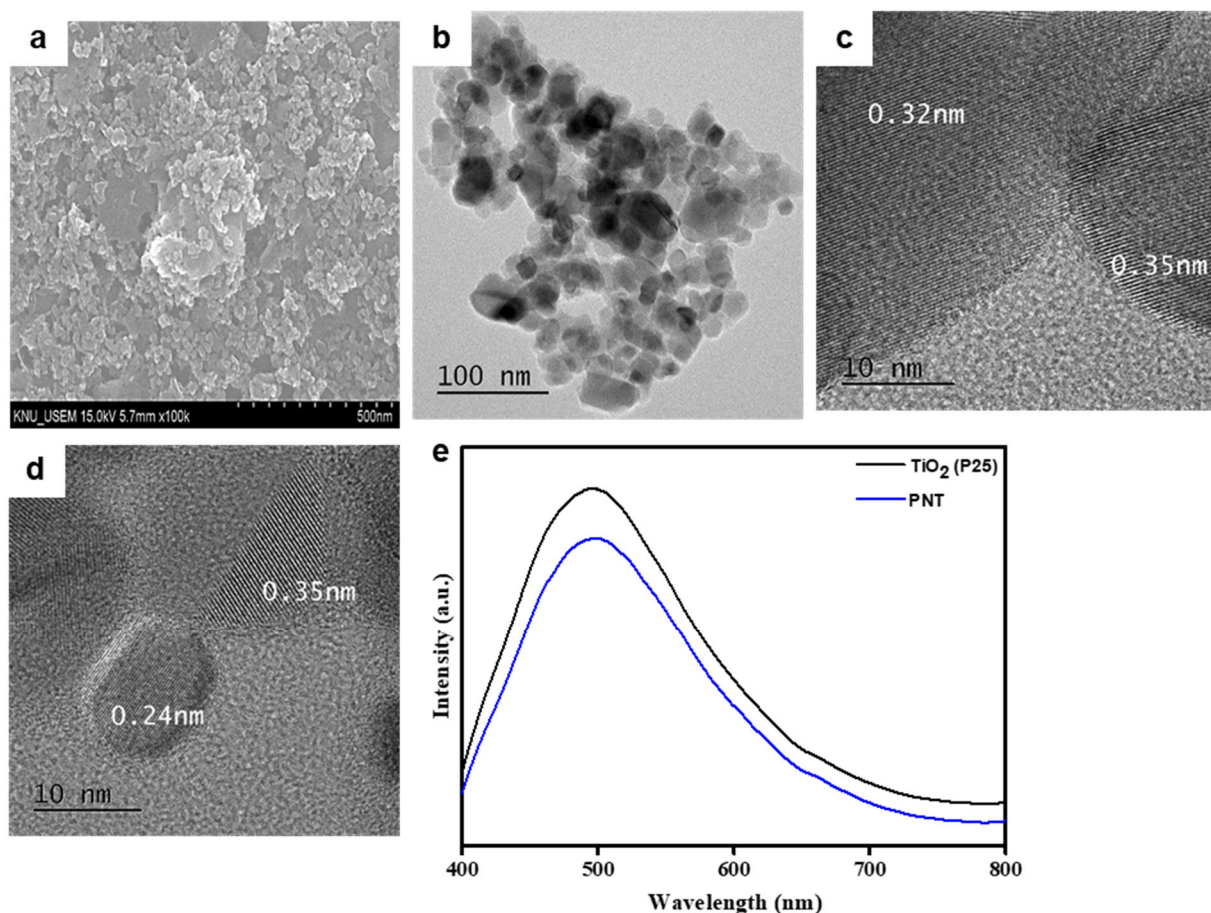


**Figure 2.** (a) SEM image of PNT on glass substrate, (b) HRTEM image of PNT, (c,d) lattice image of PNT, (e) photoluminescence spectra of PNT.

### 2.3. Crystallinity of PNT/NWPF

An XRD analysis was performed on the prepared materials to determine their crystal phase structure (Figure 3). PNT prepared from TiO<sub>2</sub> (P25) has both the anatase phase and rutile phase (in accordance with JCPDS 21-1272 and JCPDS 21-1276 standard reference pattern), which is consistent with the biphasic structure of commercial P25 [39]. Additionally, there were no other characteristic peaks from impurities as indicated by the XRD patterns. Further, PNT is coated on non-woven polymer fabric which is composed of double-layered polymer-polyethylene terephthalate (PET) fiber and polypropylene. Among the double layer, the photocatalyst PNT preferred selective coating on the polyethylene terephthalate layer only because of its superior hydrophilic nature compared to polypropylene. According to the literature, the crystal faces of high crystal PET fibers have been assigned to the

following numerous diffraction peaks positioned at  $17.5^\circ$ ,  $21.5^\circ$ , and  $26.1^\circ$  values of  $2\theta$  corresponding to 010, 110, and 100 crystal planes, respectively [40,41]. Meanwhile, the lattice plane 110 appeared at  $13.95^\circ$  represents for the polypropylene layer [42]. After the PNT coating on the non-woven polymer fabric, its XRD patterns indicated high intense crystalline peaks at  $25.47^\circ$ ,  $27.54^\circ$ ,  $38.05^\circ$ ,  $48.26^\circ$ ,  $54.15^\circ$ ,  $62.88^\circ$ , and  $69.03^\circ$  in both 1% and 2% photocatalyst-coated NWPF. There is not much difference in the intensities between 2% and 5% PNT-coated NWPF. Using Scherrer's formula, the crystallite size of synthesized materials was calculated from the half-width of anatase peak (101). The mean crystallite sizes of the 1%, 2%, and 5% PNT-coated NWPF are 13, 15, and 15.2 nm respectively.

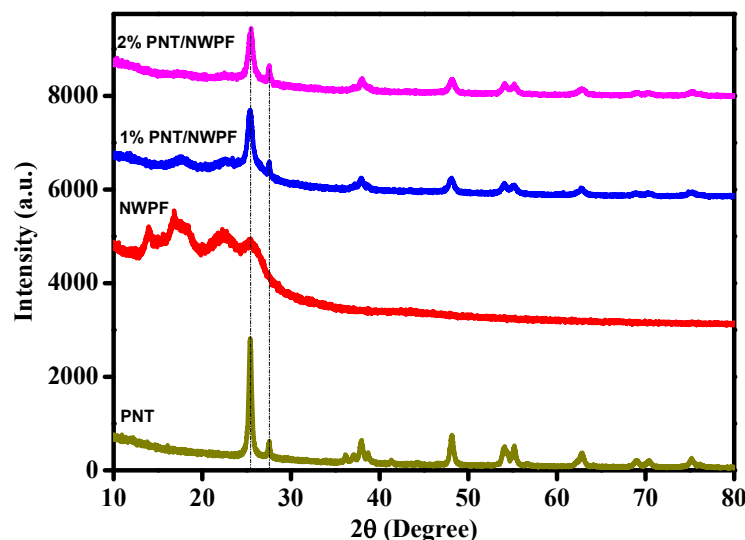


Figure 3. XRD pattern of PNT/NWPF.

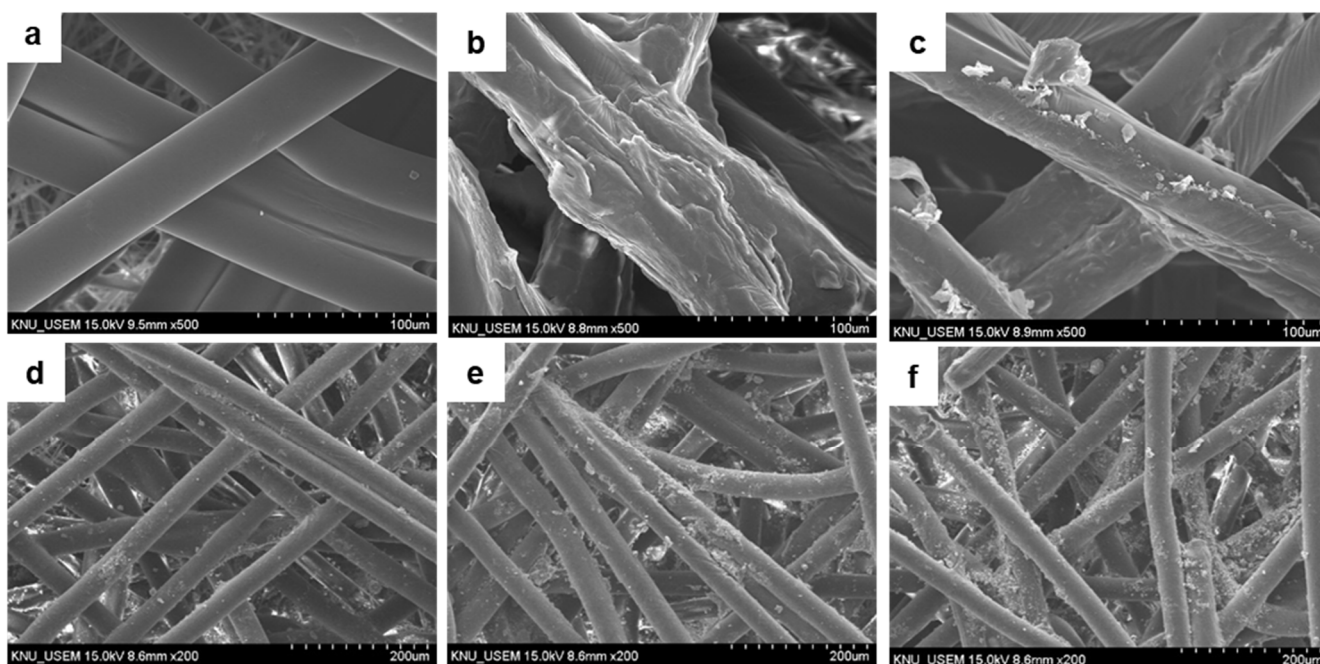
#### 2.4. Morphology of PNT Coated on NWPF

Figure 4 shows micrographs of the pristine and the visible light active photocatalyst-coated NWPFs by SEM. Figure 4a shows the long and smooth surface of pristine non-woven polymer fabric. After pretreatment, the wetting agent covers the surface of the NWPF (Figure 4b) to increase the hydrophilicity of the NWPF surface. Figure 4c shows the attachment of silica particles on the pretreated fabrics.  $\text{SiO}_2$  in water forms a hydrolysable alkoxy group which enhances hydrophilicity as well as the binding affinity of metal at the interface [43]. Figure 4d–f indicate the visible active photocatalyst with various loading amounts (1%, 2%, and 5% PNT) bound onto the non-woven fabric surface. Agglomerated PNT was seen on the surface of fabrics due to dip coating. This issue can be solved by different coating techniques such as spray and gravure coating techniques. However, the fabrics covered with fine photocatalyst nanoparticles have a high surface area with unique porosity, which improves the air filtration efficiency for removing dust, chemical, and biological contaminants [44].

#### 2.5. Coating Stability of PNT/NWPF

The different weights of PNT are coated on a  $0.005 \text{ m}^2$  area of NWPF to study its mechanical stability of the coating and maximum photocatalyst loading efficiency. The area density with different loading amounts of photocatalyst are varied from 45.8, 64.0, and  $90.1 \text{ g/m}^2$  in NWPF and labeled as sample-1, sample-2, and sample-3 in Table 1.

Sample-1, -2 and -3 represent the concentration of PNT (1, 2, and 5%) in solution, respectively. A shaking test was performed on the photocatalyst/NWPF with the SHO-2D orbital shaker to determine the mechanical strength and stability of coating. After 48 h of shaking with a maximum speed of 150 rpm, the difference in weight of the samples before and after the shaking test was measured.



**Figure 4.** SEM images of: (a) pristine NWPF, (b) pretreated NWPF, (c) SiO<sub>2</sub>-coated NWPF, (d) 1% PNT-coated NWPF, (e) 2% PNT-coated NWPF, and (f) 5% PNT-coated NWPF.

**Table 1.** Photocatalyst weight content on non-woven polymer fabric in detachment test.

Sample	Total Filter Weight after Coating Visible Active Photocatalyst			Weight Loss (%)
	Area Density before Shaking Test (g/m <sup>2</sup> )	Area Density after Shaking Test (g/m <sup>2</sup> )	Difference in Weight Loss (g/m <sup>2</sup> )	
Sample-1	45.8	45.6	0.2	0.43
Sample-2	64	63.58	0.42	0.65
Sample-3	90.1	89.1	1	1.1

The weight loss of sample-1 and -2 after 48 h was not of significant weight (<0.7%). For sample-3, noticeable weight loss (>1%) was observed. The existence of inorganic binder, SiO<sub>2</sub>, promotes the photocatalyst molecules to be strongly bonded to the NWPF surface for sample-1 and -2 [45,46]. Although the binder supports strong adherence, the weight loss would occur when the loading amount of PNT exceeds the amount required for a specific area of NWPF. The SiO<sub>2</sub>-binder-mediated dip-coating method, demonstrated in this study, provides a facile but powerful strategy to increase the stability of coatings. Moreover, it does not require high temperature and pressure and could be further extended to large-scale coatings on various polymer fabrics [47].

#### 2.6. Dust Capture Efficiency of PNT Decorated NWPF

Figure 5a shows the study of the dust collection process at various time sequences. The pristine NWPF filter has a high filtration efficiency of 96.63%. After the addition of a wetting agent, filtration efficiency rapidly decreases. This is due to the highly negatively charged sodium lauryl sulfate species (C<sub>12</sub>H<sub>25</sub>O<sub>4</sub>S<sup>−</sup>) contact with the polypropylene (PP) group of NWPF. There is a strong interaction between (C<sub>12</sub>H<sub>25</sub>O<sub>4</sub>S<sup>−</sup>) and PP which exceeds the carbon species and the original PP. Then, the wetting-agent-treated NWPF has highly-negative charge compared to the pristine NWPF. Yang et al. studied the filtration performance of fibrous filters pretreated with several ionic surfactants [48]. It has been explained that the decrease in filtration efficiency is due to the coulombic and dielectrophoretic aerosol

capture mechanism. The aerosol contains singly charged species as well as neutral species. Aerosol penetration through the sodium lauryl sulfate–treated NWPF is lower than that of pristine NWPF towards the both singly charged and neutral aerosols representing the columbic capture mechanism and dielectrophoretic mechanism directing the performance of the wetting-agent-treated NWPF. The columbic effect is dominant for the smaller aerosol ( $<0.2 \mu\text{m}$ ) and the dielectrophoretic force works at larger aerosol sizes ( $>0.2 \mu\text{m}$ ). The dielectrophoretic capture mechanism is predominant for NaCl ( $0.3 \mu\text{m}$ ). The neutral aerosols get polarized because of the dielectrophoretic effect which causes charge imbalance and reduces the filtration efficiency, but after coating 1% photocatalyst, the performance of dust capture increased greatly to 91.11%, whereas when the velocity is increased very high to  $1.3 \text{ ms}^{-1}$ , the filtration efficiency is remarkably decreased because of the fast penetration of small, fine dust particles. At a high flow rate, the particles with high speed are difficult to capture on the filter, which is controlled by various filtration mechanisms such as inertial impaction, Brownian diffusion, interception, and gravitational settling. Fine particles with a size greater than  $2.5 \mu\text{m}$  are effectively filtered through the mechanical filtration process. However, this process is not feasible for particles that are less than  $2.5 \mu\text{m}$ . In addition to mechanical filtration, the filtration efficiency of photocatalyst depends on the electrostatic charge. Pretreated NWPF has a high negative charge due to the anionic wetting agent, and it could not capture the large size particles, consistent with the reported work [49].

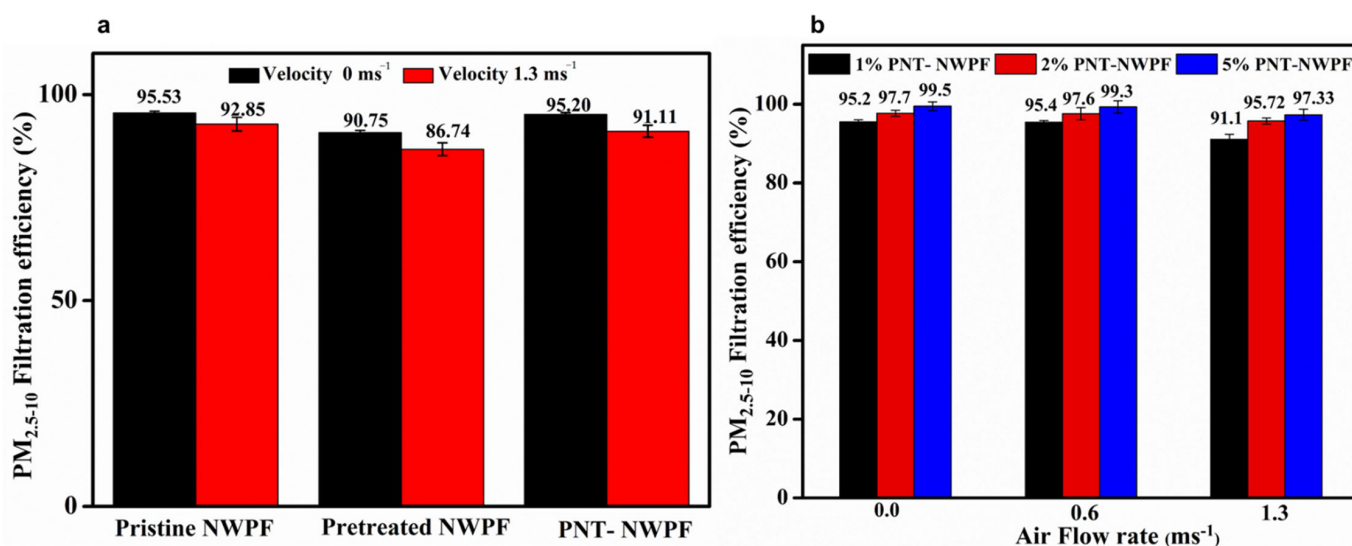


**Figure 5.** (a) Fine dust filtration efficiency at different air velocities. (b) Effect of catalyst loading efficiency.

The undesired effect of the pretreated NWPF, caused by excess negative charge, is recovered and even empowered by the loading of photocatalyst, as shown in Figure 5b. When loading of the photocatalyst is increased, the particles are strongly polarized in the fibers and the excess negative charge is neutralized, which are then adsorbed on the surface, which, in turn, increases the filtration removal efficiency [50]. The quality factor value has significant differences depending on the loading amount of photocatalyst, as shown in Table 2.

**Table 2.** Summary of filtration efficiency, pressure drop, and quality factor of PNT/NWPF air filter.

Photocatalyst	Area Density (g/m <sup>2</sup> )	Filtration Efficiency (%)	Pressure Drop (Pa <sup>-1</sup> )	Quality Factor (Pa <sup>-1</sup> )
1% PNT/NWPF	45.8	95.4	78.36	0.0393
2% PNT/NWPF	64	97.6	96.62	0.0403
5% PNT/NWPF	90.1	99.3	128.12	0.0387

The morphology of PNT/NWPF before and after the filtration test was examined using SEM. The PNT nanoparticles deposited on NWPF are shown in Figure 6a. After the continuous feed of incense smoke for 300 s, aggregated particulate matter captured on the filter is shown (Figure 6b). The inlet image of Figure 6b shows captured PM of various sizes. The data clearly shows that 2% PNT had a high optimal value of  $0.0403 \text{ Pa}^{-1}$ , which is feasible for commercial applications and also further study for VOC removal as a proof of concept.

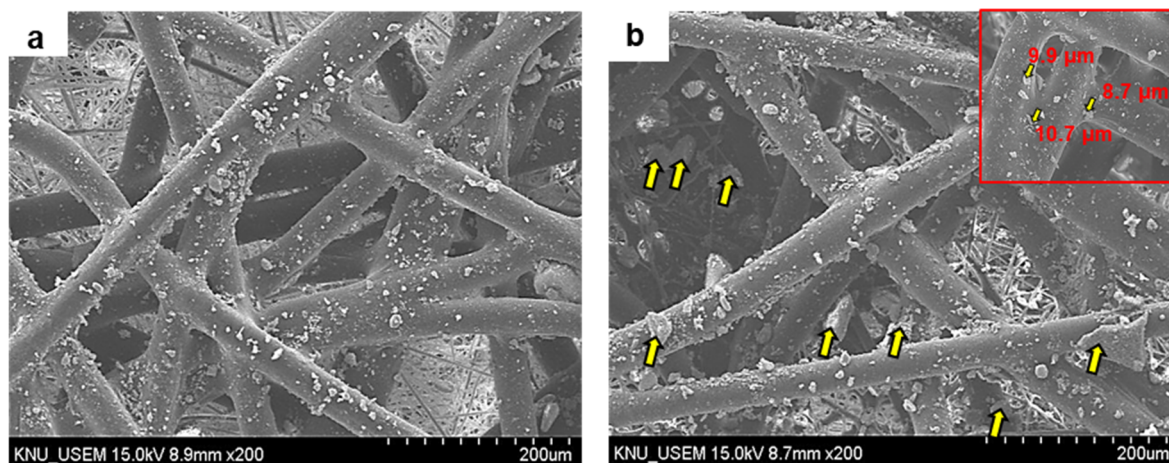


**Figure 6.** SEM images of (a) 5% PNT/NWPF before PM filtration and (b) 5%PNT/NWPF after PM filtration.

### 2.7. VOC Removal Efficiency of PNT/NWPF

The decomposition of gaseous indoor VOC is of major interest in the field of filtration, especially for the IAQ. The photocatalytic breakdown of noxious VOC *p*-xylene into carbon dioxide and water can be further demonstrated by the PNT-coated NWPF under normally visible light irradiation. The inlet concentration of *p*-xylene that is passed through the reactor remained constant at about 2 ppm, with a total airflow rate of 50 mL/min. Humidity is maintained around 50–60%. The photocatalytic activity of PNT-coated NWPF air filter for the removal of *p*-xylene pollutant is shown in Figure 7a. The concentration of the contaminant in NWPF is slightly reduced due to the adsorption, and there is no degradation in the presence or absence of light, but in the presence of visible light, the *p*-xylene levels have reduced drastically on PNT-coated NWPF, on the first single-pass of gas into the reactor in 25 min. When the loading amount of the photocatalyst is increased from 1 and 2%, the decomposition performance of the photocatalyst improved greatly. The rate of decomposition increased from 62.1 to 86.5% in the average of 100 min. The amount of photocatalyst loaded on NWPF is in the range of 45.8 to 64 g/m<sup>2</sup> for different concentrations. When higher amount of PNT is loaded on NWPF, the efficiency of photocatalyst (5% PNT/NWPF) is greatly increased to 94.2% under normal visible daylight. Limmongkona et al. also studied photocatalytic TiO<sub>2</sub>-coated air filters for the degradation of *p*-xylene, where the loading of TiO<sub>2</sub> contents influences the decomposition of pollutant *p*-xylene [51]. TiO<sub>2</sub> nanoparticles have a high surface area of 37.5 m<sup>2</sup>/g (Figure 7b) and the surface roughness with unique pores (diameter 48Å) which concomitantly contribute to the pollutant capture. In addition, they strongly induce the photocatalytic oxidation which effectively enhances the decomposition of adsorbed *p*-xylene through the capture and decompose mechanism.



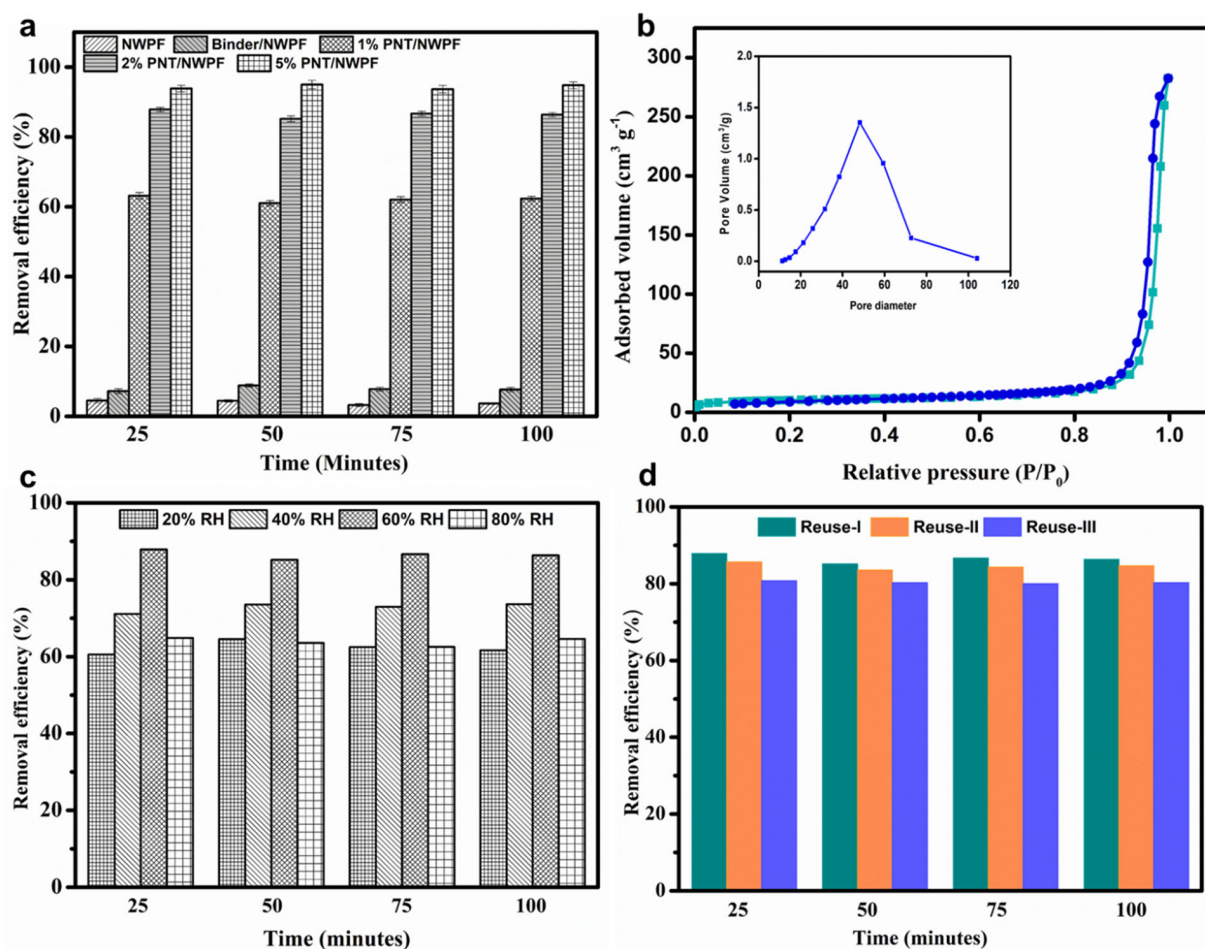


**Figure 7.** (a) VOC removal efficiency of PNT/NWPF for *p*-xylene destruction. (b) N<sub>2</sub> adsorption-desorption isotherm of PNT. (c) Effect of relative humidity on PNT/NWPF. (d) Reusability of PNT/NWPF.

The role of pristine NWPF is that it arrests only the dust particles on its surface [52]. However, PNT-coated NWPF can capture the dust particles and also enable it to decompose the VOCs under visible light. When *p*-xylene is passed into the reactor with humid air into the inlet chamber, the photocatalyst-coated NWPF is placed in the photoreactor. When the VOC contacts the photocatalyst coated NWPF, the high efficient filter capture the VOC on the photocatalyst surface. When the light is irradiated, the photocatalyst is activated by the incident photons, and the electron-hole pair is produced, which generates hydroxyl and superoxide anion radicals and degrades the *p*-xylene into carbon dioxide and water [53]. Moreover, the high surface area of the photocatalyst provides an effective platform for harvesting a large number of photos on the surface. In this study, the xylene removal performance of 2% PNT/NWPF was compared with some other progressive studies mentioned in Table 3.

**Table 3.** Photocatalytic activity of PNT/NWPF of current work and other reported literature data for xylene pollutant decomposition.

Photocatalyst	Pollutant	Light Source	Removal Efficiency (%)	Reference
5% (wt) Degussa-TiO <sub>2</sub> coated on high efficiency particulate air filter (HEPA)	xylene	36 W UV lamp	49%	[51]

Table 3. Cont.

Photocatalyst	Pollutant	Light Source	Removal Efficiency (%)	Reference
Blackened TiO <sub>2</sub>	xylene	UV+ Visible light (365–375 nm + 470–618 nm)	35.64%	[54]
TiO <sub>2</sub> , Mn-doped TiO <sub>2</sub> on Ceramic Honeycomb substrate	xylene	UV light UV <sub>254+185</sub> nm	33.5% 94%	[55]
Degussa-TiO <sub>2</sub> 0.1% Mn-TiO <sub>2</sub>	xylene	300 W UV light 300 W UV, 500 W Halogen light	58% 58% 22%	[56]
1% (wt) PNT/NWPF 2% (wt) PNT/NWPF 5% (wt) PNT/NWPF	xylene	24 W Fluorescent lamp	62.1% 86.5% 94.2%	Current work

Most of the VOCs can be decomposed more efficiently with an increase in relative humidity (RH) level. Thus, photocatalyst generates OH radicals under visible light irradiation in order to participate in VOC oxidation [57]. Water molecules (H<sub>2</sub>O) can compete with volatile organic pollutants for adsorption on active sites. The adsorption of water molecules on the PNT surface prompts the formation of the surface hydroxyl groups through the dissociation of water molecules at a certain level of relative humidity. However, at the same time, moisture adsorption can form a layer of water molecules which prevents the adsorption of VOCs onto the PNT surface [58]. Hence, photocatalytic degradation can also be influenced by moisture content, but an optimal RH level is required for maximum photocatalytic degradation. The effect of RH level on the degradation of *p*-xylene by 1%PNT/NWPF is studied by varying the RH from 20 to 80%. As can be seen from Figure 7c, as humidity increases, the removal efficiency of *p*-xylene increases rapidly, reaching a maximum removal efficiency at specific RH level and then slowly decreases at higher RH levels. When the RH increased from 20% to 60% gradually, excess hydroxyl radicals are produced that enhance the decomposition rate from 62.1% to 87.7% [59], but after the saturated point, the further increase in humidity decreases the performance of PNT/NWPF to 64.6% because when the RH level is increased to 80%, excess hydroxyl radicals occupy the photocatalyst surface, suppressing the adsorption of the pollutant *p*-xylene. In addition, water molecules may reduce the intensity of light reaching the photocatalyst surface through the dispersion of light [60–62].

The reusability of the photocatalyst is a significant factor for commercial applications. The used 2%PNT/NWPF is heated at 65 °C to remove the traces of adsorbed gases and flushed with air in the reactor for 15 min before recycle testing. The degradation of *p*-xylene is maintained in the average of 80% even after three consecutive cycles (Figure 7d). Based on these results, PNT/NWPF is proved to be an excellent air-purifying photocatalyst material that maintains a high level of photocatalytic activity and durability over a long period of time.

### 2.8. Antibacterial Activity of PNT/NWPF

The antibacterial ability of pristine and photocatalyst-coated non-woven polymer fabrics has been investigated via the colony-forming-unit (CFU) counting method. Figure 8a shows the *E. coli* colonies with the pristine non-woven polymer fabrics are much larger than the initial concentration of the colonies. The concentration of *E. coli* on 2 h light irradiation, increased from  $1 \times 10^5$  to  $3.1 \times 10^5$ . In contrast, photocatalyst-coated non-woven polymer fabric had excellent antibacterial performance, showing 99.9% destruction of bacteria (Figure 8b). The antibacterial mechanism of the photocatalyst/NWPF filter is described by observing the TEM morphology of bacterial cells before and after treatment with PNT/NWPF. Before activation with the photocatalyst, the surface of *E. coli* seemed to be granular and smooth (Figure 8c). When a bacteria cell is exposed to photocatalyst

under visible light for an extended period of time, it loses its smooth, tight surface texture. After treatment with PNT/NWPF under visible light, disruption in the cell membrane causing the leakage of cell contents leads to cell death (Figure 8d) [63]. In other words, the photocatalyst absorbs the visible light making the electrons excited and jumps from the valence band to its conduction band. The photo-generated electrons on the conduction band react with oxygen and water to form hydroxyl and superoxide radicals [64]. The reactive oxygen species ( $^{\ominus}\text{O}_2$  and  $\cdot\text{OH}$ ) oxidize, which initially attacks the polyunsaturated phospholipid outer layer and disintegrates the cytoplasmic membrane, leading to the leakage of intracellular constituents such as proteins and lipids and causes the death of the bacteria [65].

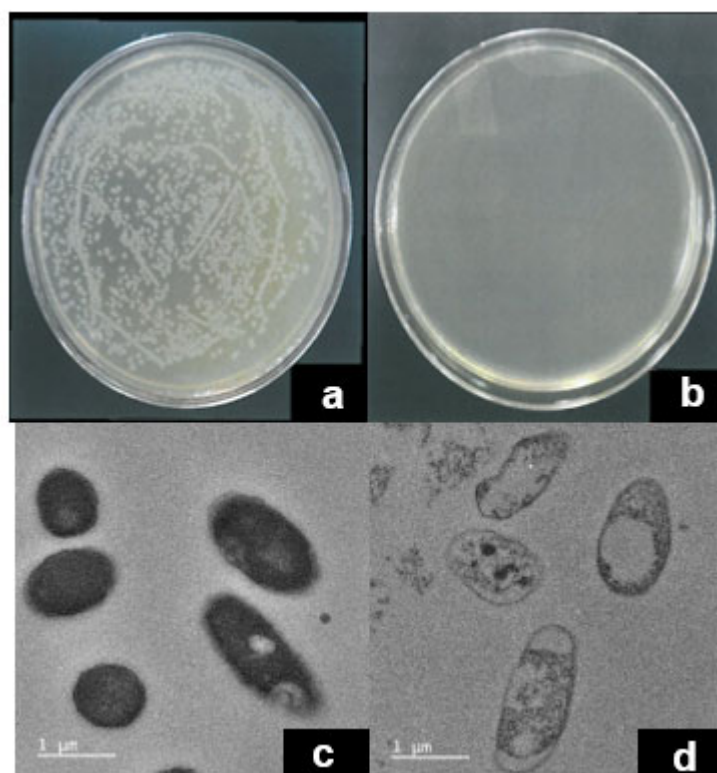


**Figure 8.** Bacterial disinfection image of (a) NWPF, (b) PNT/NWPF after 2 h treatment. TEM images of *E. coli*, (c) before inactivation with PNT and (d) after inactivation with PNT.

### 3. Materials and Methods

#### 3.1. Materials

Degussa P25 titanium dioxide, Ludox colloidal silica, and urea were purchased from Sigma Aldrich. Sodium dodecyl sulfate was provided by Georgia chem. The analytical grade reagents such as ammonia and isopropyl alcohol were received from Daejung chemicals. All the Gram-negative strain *E. coli* was provided by Real Biotech Corporation (Taiwan). MilliQ water was used for all experiments.

#### 3.2. Preparation of PNT

About 0.5 g of titanium dioxide (Degussa P25) is added to 45 mL distilled water in a round-bottomed flask, and 5 mL of 2.5% ammonium hydroxide solution is added dropwise under slow stirring. Then, urea (0.1 M) dissolved in water/IPA mixture (1:1) and added to the above solution gradually and stirred for 15 min. The mixture is evaporated for 2 h, cooled, and oven-dried at 50 °C overnight. The powder is ground well and calcined at 400 °C for 3 h. The final product photocatalyst nitrogen-doped titanium dioxide (PNT) nanoparticles is obtained. Different concentrations of PNT (1%, 2%, and 5% wt) is prepared in hot water and is sonicated for 15 min and used for coating on NWPF substrate.

### 3.3. Fabrication of PNT/NWPF Air Filter

Pretreatment of NWPF substrate: NWPF of grade H13 was received from Easy Rental Networks Ltd., (Seoul, Republic of Korea). The hydrophilicity of NWPF for PNT coating was enhanced after pretreatment process [66]. To improve the hydrophilicity of NWPF, surfactant 0.01 M Sodium dodecyl sulfate (SDS) was used as wetting agent, where the NWPF was immersed in SDS solution, air-dried, and baked at 50 °C for 30 min.

Coating procedure: NWPF was immersed in 0.1% silica stabilizer/binder for 10 min, air-dried, and baked for another 15 min. Silica binder helps for strong adherence coating of PNT and also has a high porous structure. This pretreated NWPF was dipped in PNT suspension for 10 min, air-dried, and further oven-dried at 50 °C. The loading of PNT is increased by number of dipping times.

### 3.4. Dust Capture ( $PM_{2.5-10}$ ) Experiment

The experimental setup for analyzing the particulate fine matter is shown in Figure 9. For the generation of fine particles, incense is burned, which contains high particle density. The smoke generated from incense has a fine particulate matter with a wide distribution from <300 nm to >10  $\mu\text{m}$ , with a minimum mass concentration of 5000  $\mu\text{g}/\text{cm}^2$ . The generated particulate matter is filled into the inlet chamber (optical particle sizer, Model-3330, TSI). The photocatalyst air filter is placed between two chambers (inlet and outlet). The concentration of  $PM_{2.5-10}$  concentration is measured at both inlet and outlet chamber with respect to time and measured through a laser PM counter device (Wuhan Cubic Optoelectronics Co. Ltd., PM2005 (Wuhan, China)). Anemometer is used to analyze the capture efficiency of particulate matter under different air flow rates. The removal efficiency of the filters is calculated with the following.

$$\eta = ([C_{\text{Inlet}} - C_{\text{Outlet}}]/[C_{\text{Inlet}}]) \times 100$$

where  $\eta$  is the  $PM_{2.5-10}$  capture efficiency, ' $C_{\text{Inlet}}$ ', and ' $C_{\text{Outlet}}$ ' are the mass concentrations of particulates at inlet and outlet chambers. Pressure drop ( $\Delta p$ ) is measured using pressure gauge (Manometer, Bluewind Lab (Choa Chu Kang, Singapore)). In order to be effective commercial air filter material, the filter should have a high filtration efficiency and a low pressure drop. The quality factor (QF) incorporates both of these aforementioned factors into a single parameter. Quality factor [ $QF = -\ln(1 - \eta)/\Delta p$ ] is also determined to evaluate the filtration capacity of air filters based on their removal efficiency.

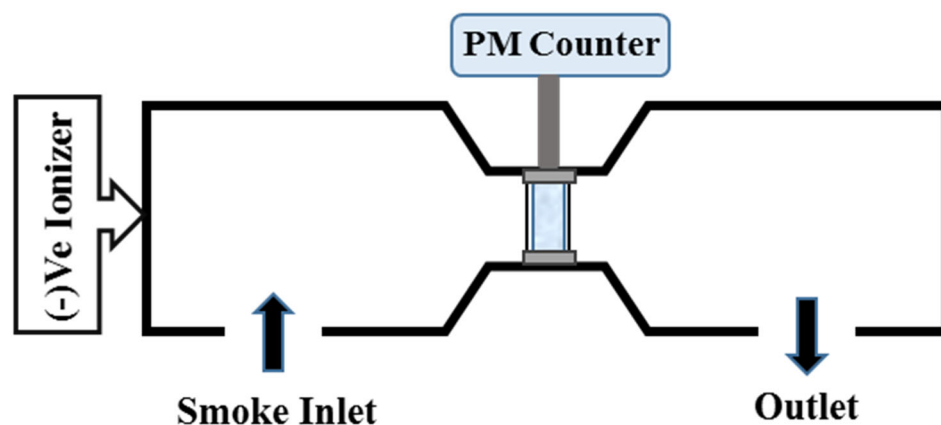
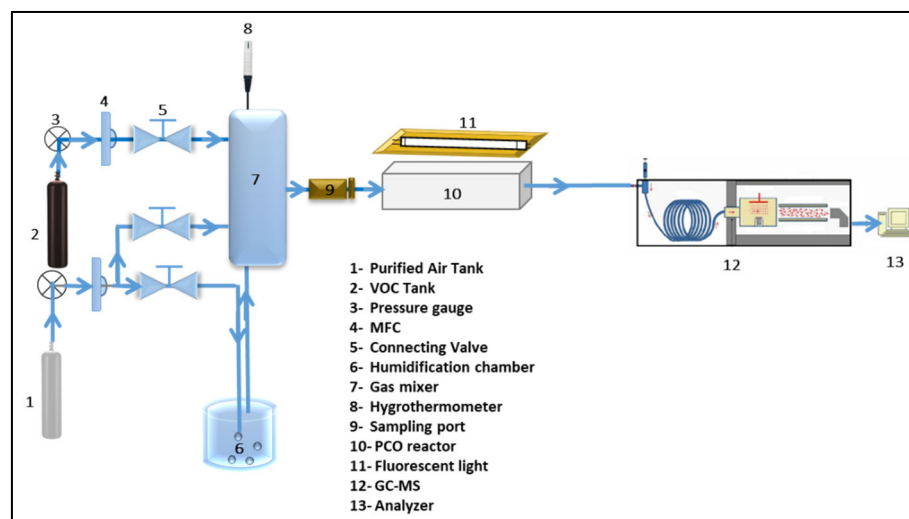


Figure 9. Schematic diagram of PM filtration equipment.

### 3.5. Experiment for Photocatalytic Oxidation

In accordance with the ISO standard 22197-1, the fixed-bed photoreactor is developed with unique changes. The body of the vessel is made of stainless steel of dimension 390 × 90 × 40 mm (CHEMRE SYSTEM, Republic of Korea), which reduced pollutant ad-

sorption within the reactor. On the top cover of the reactor vessel, an optical GE 214 quartz glass is mounted with ultra-low resistance to UV light. Before and after each experimental cycle a leak test is conducted. The photocatalytic oxidation (PCO) experimental set-up schematic diagram is shown in Figure 10. To test various and different concentration of samples simultaneously under the same reaction conditions, two parallel reactors are used. Three wavelength covering (400–700 nm) 24 W fluorescent light tubes widely used for residential applications is employed.



**Figure 10.** Schematic diagram of PCO reactor.

The fluorescent light tube is mounted with fixed distance of 3 cm to the surface of the reactor. Synthetic purified air as the carrier gas to transport pollutant *p*-xylene and water vapor (humidification device) into the mixing compartment with varying mixing ratios are regulated by the volumetric flow meter. Gaseous pollutant *p*-xylene (50 ppm/100 bar N<sub>2</sub>) was purchased from Seoul Specialty Gas Co Ltd (Seoul, Republic of Korea). Following a normal protocol, the PCO studies are conducted out. First, under the absence of light conditions, the test gas combined with humidity continuously circulated through the reactor until the test sample reached steady state condition, which further is analyzed by attaining equal pollutant concentrations at the reactor inlet ( $C_{\text{Inlet}}$ ) and outlet ( $C_{\text{Outlet}}$ ). The degradation efficacy of VIS-PCO of *p*-xylene is determined by:

$$\% \text{ of Pollutant degradation} = [1 - (p\text{-xylene } C_{\text{Outlet}} / p\text{-xylene } C_{\text{Inlet}})] \times 100$$

### 3.6. Antibacterial Application of PNT/NWPF

Typically, the PNT/NWPF filter (with size 2.5 cm × 2.5 cm × 1.0 cm) is immersed in a bottle containing a mixture of 20 mL PBS and 200 μL pathogen solution ( $1.4 \times 10^5$  CFU mL<sup>-1</sup>). The mixture is shaken and incubated at 37 °C and 230 rpm. The fluorescent light is kept at a distance of 35 cm from the test sample. As the reaction continued, the sample is pipetted out after 2 h and distributed in sterilized glass tubes containing a 10 mL saline solution by a ten-fold serial dilution method. Then, 100 μL of the solution are plated on a plate count agar medium and incubated at 37 °C for 48 h. Subsequently, the live cells are counted to obtain the results for the disinfection performance. In a similar way, NWPF is also tested under same conditions to evaluate its disinfection. Each experiment is repeated three times.

$$\text{Destruction Efficiency} = \frac{(\text{Conc}_0 - \text{Conc})}{\text{Conc}_0} \quad (1)$$

where “Conc<sub>0</sub>” (CFU/ mL) presents *E. coli* concentration in the absence of photocatalyst and “Conc” stand for concentration of microorganisms in presence of photocatalyst after 2 h.

### 3.7. Materials Characterization

Absorption spectra was obtained for PNT nanoparticles using Diffuse Reflectance UV-VIS-NIR Spectrophotometer (Shimadzu SolidSpec-3700). Morphology of photocatalyst coated NWPF was analyzed by scanning electron microscope (SEM, Hitachi S-4800). Crystallinity of PNT/NWPF analysis was conducted using high-resolution X-ray diffractometer (X'Pert PRO MPD) with Cu radiation. The average crystallite size is calculated using Scherrer formula [ $D = k\lambda/W\cos\theta$ ] in which  $k$  is the numerical constant ( $k = 0.93$ ),  $\lambda$  is CuK $\alpha$  wavelength ( $\lambda = 1.5406 \text{ \AA}$ ). The elemental analysis is carried out using X-ray photoelectron spectroscopy (Thermo VG K Alpha+), and the atomic weight (%) of doped nitrogen in the PNT was 2.6%. Nitrogen adsorption/desorption measurement was performed to analyze the surface area of photocatalyst PNT using Micrometrics instrument (ASAP 2420). TEM analysis for the bacteria samples was photographed by HR-TEM (JEOL-JSM 1200EX, Tokyo, Japan).

## 4. Conclusions

PNT is prepared as an efficient visible photocatalyst by modifying titanium dioxide (Degussa P25) with urea as nitrogen precursor by simple thermal condensation method. Using the dip-coating procedure, PNT is decorated on NWPF. The agglomerated PNT nanoparticles is seen in SEM images. The role of silica binder on PNT/NWPF ensures the strong stability of coating, which is highlighted from the detachment test results. The high dust capture efficiency of the PNT-coated fabrics is evaluated. For the feasibility of coating, non-woven polymer fabric is pretreated with a wetting agent. So, the filtration efficiency is decreased due to charge effect. This is compensated by the higher loading amount of photocatalyst PNT. The major emitting pollutant from the industrial sectors in South Korea is xylene, which was selected as the pollutant model for testing the photocatalytic activity of PNT. The filter composed of PNT/NWPF showed 5.5 times greater activity than P25 and could efficiently degrade para-xylene under normal visible light irradiation, thus developing an air filter (PNT-coated NWPF) which has multi-functional purpose. Based on this study, a conceptual air purifier containing a multi-functional filter such as PNT/NWPF, active under normal white fluorescent daylight, can be designed, which will pave the way for a better future in indoor air purification applications.

**Author Contributions:** Conceptualization, methodology, V.P.; Writing—original draft preparation, P.P.S.; Formal analysis, M.S.; Investigation, T.Y.P.; review and writing, H.L.; Supervision, W.R.L.; Project administration, funding acquisition, supervision, S.K. All authors have read and agreed to the published version of the manuscript.

**Funding:** This work is financially supported by the Korea Ministry of Environment as Waste to Energy-Recycling Human Resource Development Project (YL-WE-21-001).

**Data Availability Statement:** The data presented in this study are available in the article.

**Acknowledgments:** All the authors extend their thanks to Seungdo Kim for giving this research opportunity.

**Conflicts of Interest:** The authors declare no conflict of interest.

## References

1. Hargreaves, M.; Parappukkaran, S.; Morawska, L.; Hitchins, J.; He, C.; Gilbert, D. A pilot investigation into associations between indoor airborne fungal and non-biological particle concentrations in residential houses in Brisbane, Australia. *Sci. Total Environ.* **2003**, *312*, 89–101. [[CrossRef](#)]
2. Zhang, J.F.; Smith, K.R. Indoor air pollution: A global health concern. *Br. Med. Bull.* **2003**, *68*, 209–225. [[CrossRef](#)] [[PubMed](#)]
3. Maggos, T.; Binas, V.; Siaperas, V.; Terzopoulos, A.; Panagopoulos, P.; Kiriakidis, G. A Promising Technological Approach to Improve Indoor Air Quality. *Appl. Sci.* **2019**, *9*, 4837. [[CrossRef](#)]
4. Suryadhi, M.A.H.; Abudureyimu, K.; Kashima, S.; Yorifuji, T. Effects of Household Air Pollution From Solid Fuel Use and Environmental Tobacco Smoke on Child Health Outcomes in Indonesia. *J. Occup. Environ. Med.* **2019**, *61*, 335–339. [[CrossRef](#)]
5. Wickliffe, J.K.; Stock, T.H.; Howard, J.L.; Frahm, E.; Simon-Friedt, B.R.; Montgomery, K.; Wilson, M.J.; Lichtveld, M.Y.; Harville, E. Increased long-term health risks attributable to select volatile organic compounds in residential indoor air in southeast Louisiana. *Sci. Rep.* **2020**, *10*, 21649. [[CrossRef](#)]

6. Guo, P.; Yokoyama, K.; Piao, F.; Sakai, K.; Khalequzzaman, M.; Kamijima, M.; Nakajima, T.; Kitamura, F. Sick building syndrome by indoor air pollution in Dalian, China. *Int. J. Environ. Res. Public Health* **2013**, *10*, 1489–1504. [[CrossRef](#)] [[PubMed](#)]
7. Nakaoka, H.; Todaka, E.; Seto, H.; Saito, I.; Hanazato, M.; Watanabe, M.; Mori, C. Correlating the symptoms of sick-building syndrome to indoor VOCs concentration levels and odour. *Indoor Built Environ.* **2014**, *23*, 804–813. [[CrossRef](#)]
8. Todaka, E.; Nakaoka, H.; Hanazato, M.; Seto, H.; Mori, C. Sick building syndrome and total volatile organic compounds. *Toxicol. Lett.* **2012**, *211*, S94. [[CrossRef](#)]
9. Im, J.; Kim, B.; Kim, H.; Lee, M.; Jeon, D.; Ryu, J.; Yun, D.; Jang, Y.; Lee, C. A Study on the Characteristics of Hazardous Pollutant Emissions in Korea from 2007 to 2016. *Int. J. Environ. Res.* **2020**, *14*, 335–346. [[CrossRef](#)]
10. Li, X.; Zhou, Q.; Luo, Y.; Yang, G.; Zhou, T. Joint action and lethal levels of toluene, ethylbenzene, and xylene on midge (*Chironomus plumosus*) larvae. *Environ. Sci. Pollut. Res.* **2013**, *20*, 957–966. [[CrossRef](#)]
11. Sriprapat, W.; Suksabye, P.; Areephak, S.; Klantup, P.; Waraha, A.; Sawattan, A.; Thiravetyan, P. Uptake of toluene and ethylbenzene by plants: Removal of volatile indoor air contaminants. *Ecotoxicol. Environ. Saf.* **2014**, *102*, 147–151. [[CrossRef](#)] [[PubMed](#)]
12. Niaz, K.; Bahadar, H.; Maqbool, F.; Abdollahi, M. A review of environmental and occupational exposure to xylene and its health concerns. *EXCLI J.* **2015**, *14*, 1167–1186. [[CrossRef](#)] [[PubMed](#)]
13. Bang, J.-H.; Oh, I.; Kim, S.; You, S.; Kim, Y.; Kwon, H.-J.; Kim, G.-B. Modeling the effects of pollutant emissions from large industrial complexes on benzene, toluene, and xylene (BTX) concentrations in urban areas. *Environ. Health Toxicol.* **2017**, *32*, e2017022. [[CrossRef](#)] [[PubMed](#)]
14. Kapilan, N.; Rao, L.N. COVID-19 and importance of air filtration. *Diabetes Metab. Syndr. Clin. Res. Rev.* **2021**, *15*, 102183. [[CrossRef](#)] [[PubMed](#)]
15. Dubey, S.; Rohra, H.; Taneja, A. Assessing effectiveness of air purifiers (HEPA) for controlling indoor particulate pollution. *Heliyon* **2021**, *7*, e07976. [[CrossRef](#)] [[PubMed](#)]
16. Xia, X.; Chan, K.H.; Lam, K.B.H.; Qiu, H.; Li, Z.; Yim, S.H.L.; Ho, K.-F. Effectiveness of indoor air purification intervention in improving cardiovascular health: A systematic review and meta-analysis of randomized controlled trials. *Sci. Total Environ.* **2021**, *789*, 147882. [[CrossRef](#)]
17. Ren, H.; Koshy, P.; Chen, W.-F.; Qi, S.; Sorrell, C.C. Photocatalytic materials and technologies for air purification. *J. Hazard. Mater.* **2017**, *325*, 340–366. [[CrossRef](#)]
18. Hu, S.; Jin, L.; Si, W.; Wang, B.; Zhu, M. Sulfur Vacancies Enriched 2D ZnIn<sub>2</sub>S<sub>4</sub> Nanosheets for Improving Photoelectrochemical Performance. *Catalysts* **2022**, *12*, 400. [[CrossRef](#)]
19. Liu, B.; Zhang, M.; Yang, J.; Zhu, M. Efficient ozone decomposition over bifunctional Co<sub>3</sub>Mn-layered double hydroxide with strong electronic interaction. *Chin. Chem. Lett.* **2022**, *33*, 4679–4682. [[CrossRef](#)]
20. Taranto, J.; Frochot, D.; Pichat, P. Photocatalytic air purification: Comparative efficacy and pressure drop of a TiO<sub>2</sub>-coated thin mesh and a honeycomb monolith at high air velocities using a 0.4 m<sup>3</sup> close-loop reactor. *Sep. Purif. Technol.* **2009**, *67*, 187–193. [[CrossRef](#)]
21. Andersen, B.M.; Bånrud, H.; Bøe, E.; Bjordal, O.; Drangsholt, F. Comparison of UV C light and chemicals for disinfection of surfaces in hospital isolation units. *Infect. Control Hosp. Epidemiol.* **2006**, *27*, 729–734. [[CrossRef](#)] [[PubMed](#)]
22. Cheng, Z.; Quan, X.; Xiang, J.; Huang, Y.; Xu, Y. Photocatalytic degradation of bisphenol A using an integrated system of a new gas-liquid-solid circulating fluidized bed reactor and micrometer Gd-doped TiO<sub>2</sub> particles. *J. Environ. Sci.* **2012**, *24*, 1317–1326. [[CrossRef](#)]
23. Xi, G.; Ouyang, S.; Ye, J. General Synthesis of Hybrid TiO<sub>2</sub> Mesoporous “French Fries” Toward Improved Photocatalytic Conversion of CO<sub>2</sub> into Hydrocarbon Fuel: A Case of TiO<sub>2</sub>/ZnO. *Chemistry* **2011**, *17*, 9057–9061. [[CrossRef](#)] [[PubMed](#)]
24. Chang, X.; Wang, T.; Zhang, P.; Zhang, J.; Li, A.; Gong, J. Enhanced Surface Reaction Kinetics and Charge Separation of p-n Heterojunction Co<sub>3</sub>O<sub>4</sub>/BiVO<sub>4</sub> Photoanodes. *J. Am. Chem. Soc.* **2015**, *137*, 8356–8359. [[CrossRef](#)] [[PubMed](#)]
25. Martin, D.J.; Liu, G.; Moniz, S.J.A.; Bi, Y.; Beale, A.M.; Ye, J.; Tang, J. Efficient visible driven photocatalyst, silver phosphate: Performance, understanding and perspective. *Chem. Soc. Rev.* **2015**, *44*, 7808–7828. [[CrossRef](#)]
26. Ma, X.; Lv, Y.; Xu, J.; Liu, Y.; Zhang, R.; Zhu, Y. A Strategy of Enhancing the Photoactivity of g-C<sub>3</sub>N<sub>4</sub> via Doping of Nonmetal Elements: A First-Principles Study. *J. Phys. Chem. C* **2012**, *116*, 23485–23493. [[CrossRef](#)]
27. Khan, T.T.; Bari, G.A.R.; Kang, H.J.; Lee, T.G.; Park, J.W.; Hwang, H.J.; Hossain, S.M.; Mun, J.S.; Suzuki, N.; Fujishima, A.; et al. Synthesis of N-Doped TiO<sub>2</sub> for Efficient Photocatalytic Degradation of Atmospheric NO<sub>x</sub>. *Catalysts* **2021**, *11*, 109. [[CrossRef](#)]
28. Kim, T.H.; Go, G.-M.; Cho, H.-B.; Song, Y.; Lee, C.-G.; Choa, Y.-H. A Novel Synthetic Method for N Doped TiO<sub>2</sub> Nanoparticles Through Plasma-Assisted Electrolysis and Photocatalytic Activity in the Visible Region. *Front. Chem.* **2018**, *6*, 458. [[CrossRef](#)]
29. Kong, X.; Peng, Z.; Jiang, R.; Jia, P.; Feng, J.; Yang, P.; Chi, Q.; Ye, W.; Xu, F.; Gao, P. Nanolayered Heterostructures of N-Doped TiO<sub>2</sub> and N-Doped Carbon for Hydrogen Evolution. *ACS Appl. Nano Mater.* **2020**, *3*, 1373–1381. [[CrossRef](#)]
30. He, Q.; Sun, Z.; Shi, X.; Wu, W.; Cheng, J.; Zhuo, R.; Zhang, Z.; Wang, J. Electrochemical Performance Enhancement of Nitrogen-Doped TiO<sub>2</sub> for Lithium-Ion Batteries Investigated by a Film Electrode Model. *Energy Fuels* **2021**, *35*, 2717–2726. [[CrossRef](#)]
31. Cheng, X.; Yu, X.; Xing, Z.; Yang, L. Synthesis and characterization of N-doped TiO<sub>2</sub> and its enhanced visible-light photocatalytic activity. *Arab. J. Chem.* **2016**, *9*, S1706–S1711. [[CrossRef](#)]
32. Natarajan, T.S.; Mozhiarasi, V.; Tayade, R.J. Nitrogen Doped Titanium Dioxide (N-TiO<sub>2</sub>): Synopsis of Synthesis Methodologies, Doping Mechanisms, Property Evaluation and Visible Light Photocatalytic Applications. *Photochem* **2021**, *1*, 371–410. [[CrossRef](#)]

33. Peng, F.; Cai, L.; Yu, H.; Wang, H.; Yang, J. Synthesis and characterization of substitutional and interstitial nitrogen-doped titanium dioxides with visible light photocatalytic activity. *J. Solid State Chem.* **2008**, *181*, 130–136. [[CrossRef](#)]
34. Ji, T.; Liu, Q.; Zou, R.; Zhang, Y.; Wang, L.; Sang, L.; Liao, M.; Hu, J. Enhanced UV-visible light photodetectors with a TiO<sub>2</sub>/Si heterojunction using band engineering. *J. Mater. Chem. C* **2017**, *5*, 12848–12856. [[CrossRef](#)]
35. Batalović, K.; Bundaleski, N.; Radaković, J.; Abazović, N.; Mitrić, M.; Silva, R.A.; Savić, M.; Belošević-Čavor, J.; Rakočević, Z.; Rangel, C.M. Modification of N-doped TiO<sub>2</sub> photocatalysts using noble metals (Pt, Pd)—A combined XPS and DFT study. *Phys. Chem. Chem. Phys.* **2017**, *19*, 7062–7071. [[CrossRef](#)] [[PubMed](#)]
36. Giannakopoulou, T.; Papailias, I.; Todorova, N.; Boukos, N.; Liu, Y.; Yu, J.; Trapalis, C. Tailoring the energy band gap and edges' potentials of g-C<sub>3</sub>N<sub>4</sub>/TiO<sub>2</sub> composite photocatalysts for NO<sub>x</sub> removal. *Chem. Eng. J.* **2017**, *310*, 571–580. [[CrossRef](#)]
37. Zhang, Z.-L.; Li, J.-F.; Wang, X.-L.; Qin, J.-Q.; Shi, W.-J.; Liu, Y.-F.; Gao, H.-P.; Mao, Y.-L. Enhancement of Perovskite Solar Cells Efficiency using N-Doped TiO<sub>2</sub> Nanorod Arrays as Electron Transfer Layer. *Nanoscale Res. Lett.* **2017**, *12*, 43. [[CrossRef](#)]
38. Le, P.H.; Hieu, L.T.; Lam, T.-N.; Hang, N.T.N.; Truong, N.V.; Tuyen, L.T.C.; Phong, P.T.; Leu, J. Enhanced Photocatalytic Performance of Nitrogen-Doped TiO<sub>2</sub> Nanotube Arrays Using a Simple Annealing Process. *Micromachines* **2018**, *9*, 618. [[CrossRef](#)] [[PubMed](#)]
39. Isari, A.A.; Hayati, F.; Kakavandi, B.; Rostami, M.; Motevassel, M.; Dehghanifard, E.N. Cu co-doped TiO<sub>2</sub>@functionalized SWCNT photocatalyst coupled with ultrasound and visible-light: An effective sono-photocatalysis process for pharmaceutical wastewaters treatment. *Chem. Eng. J.* **2020**, *392*, 123685. [[CrossRef](#)]
40. Alexiou, V.F.; Mathioudakis, G.N.; Andrikopoulos, K.S.; Soto Beobide, A.; Voyiatzis, G.A. Poly(ethylene Terephthalate) Carbon-Based Nanocomposites: A Crystallization and Molecular Orientation Study. *Polymers* **2020**, *12*, 2626. [[CrossRef](#)]
41. Pulido, B.A.; Habboub, O.S.; Aristizabal, S.L.; Szekely, G.; Nunes, S.P. Recycled Poly(ethylene terephthalate) for High Temperature Solvent Resistant Membranes. *ACS Appl. Polym. Mater.* **2019**, *1*, 2379–2387. [[CrossRef](#)]
42. Zhang, H.; Liu, N.; Zeng, Q.; Liu, J.; Zhang, X.; Ge, M.; Zhang, W.; Li, S.; Fu, Y.; Zhang, Y. Design of Polypropylene Electret Melt Blown Nonwovens with Superior Filtration Efficiency Stability through Thermally Stimulated Charging. *Polymers* **2020**, *12*, 2341. [[CrossRef](#)] [[PubMed](#)]
43. Luo, Y.; Wang, L.; Hwang, Y.; Yu, J.; Lee, J.; Liu, Y.; Wang, H.; Kim, J.; Song, H.Y.; Lee, H. Binder-free TiO<sub>2</sub> hydrophilic film covalently coated by microwave treatment. *Mater. Chem. Phys.* **2021**, *258*, 123884. [[CrossRef](#)] [[PubMed](#)]
44. Deng, Y.; Lu, T.; Cui, J.; Keshari Samal, S.; Xiong, R.; Huang, C. Bio-based electrospun nanofiber as building blocks for a novel eco-friendly air filtration membrane: A review. *Sep. Purif. Technol.* **2021**, *277*, 119623. [[CrossRef](#)]
45. Magnone, E.; Kim, M.-K.; Lee, H.J.; Park, J.H. Testing and substantial improvement of TiO<sub>2</sub>/UV photocatalysts in the degradation of Methylene Blue. *Ceram. Int.* **2019**, *45*, 3359–3367. [[CrossRef](#)]
46. Pierpaoli, M.; Zheng, X.; Bondarenko, V.; Fava, G.; Ruello, M.L. Paving the Way for A Sustainable and Efficient SiO<sub>2</sub>/TiO<sub>2</sub> Photocatalytic Composite. *Environments* **2019**, *6*, 87. [[CrossRef](#)]
47. Tang, X.; Yan, X. Dip-coating for fibrous materials: Mechanism, methods and applications. *J. Sol-Gel Sci. Technol.* **2017**, *81*, 378–404. [[CrossRef](#)]
48. Yang, S.; Lee, G.W. Electrostatic enhancement of collection efficiency of the fibrous filter pretreated with ionic surfactants. *J. Air Waste Manag. Assoc.* **2005**, *55*, 594–603. [[CrossRef](#)]
49. Yang, S.; Lee, G. Filtration characteristics of a fibrous filter pretreated with anionic surfactants for monodisperse solid aerosols. *J. Aerosol Sci.* **2005**, *36*, 419–437. [[CrossRef](#)]
50. Chuaybamroong, P.; Chotigawin, R.; Supothina, S.; Sribenjalux, P.; Larpkittaworn, S.; Wu, C.Y. Efficacy of photocatalytic HEPA filter on microorganism removal. *Indoor Air* **2010**, *20*, 246–254. [[CrossRef](#)]
51. Limmongkon, Y.; Johns, J.; Charerntanyarak, L. Preparation of a TiO<sub>2</sub> -coated photocatalytic air filter for use with an electrostatic air filter pack for xylene removal. *Scienceasia* **2013**, *39*, 284. [[CrossRef](#)]
52. Mukhopadhyay, A. Composite nonwovens in filters: Applications. In *Composite Non-Woven Materials*; Woodhead Publishing: Sawston, UK, 2014; pp. 164–210. [[CrossRef](#)]
53. Han, Z.; Chang, V.; Wang, X.; Lim, T.; Hildemann, L. Experimental study on visible-light induced photocatalytic oxidation of gaseous formaldehyde by polyester fiber supported photocatalysts. *Chem. Eng. J.* **2013**, *218*, 9–18. [[CrossRef](#)]
54. Zhou, W.; Shen, B.; Wang, F.; Zhang, X.; Zhao, Z.; Si, M.; Guo, S. Enhanced photocatalytic degradation of xylene by blackening TiO<sub>2</sub> nanoparticles with high dispersion of CuO. *J. Hazard. Mater.* **2020**, *391*, 121642. [[CrossRef](#)] [[PubMed](#)]
55. Wu, Y.-T.; Yu, Y.-H.; Nguyen, V.-H.; Lu, K.-T.; Wu, J.C.-S.; Chang, L.-M.; Kuo, C.-W. Enhanced xylene removal by photocatalytic oxidation using fiber-illuminated honeycomb reactor at ppb level. *J. Hazard. Mater.* **2013**, *262*, 717–725. [[CrossRef](#)]
56. Binas, V.; Stefanopoulos, V.; Kiriakidis, G.; Papagiannakopoulos, P. Photocatalytic oxidation of gaseous benzene, toluene and xylene under UV and visible irradiation over Mn-doped TiO<sub>2</sub> nanoparticles. *J. Mater.* **2019**, *5*, 56–65. [[CrossRef](#)]
57. Pichat, P. Some views about indoor air photocatalytic treatment using TiO<sub>2</sub>: Conceptualization of humidity effects, active oxygen species, problem of C1–C3 carbonyl pollutants. *Appl. Catal. B Environ.* **2010**, *99*, 428–434. [[CrossRef](#)]
58. Nosaka, Y.; Nosaka, A.Y. Generation and Detection of Reactive Oxygen Species in Photocatalysis. *Chem. Rev.* **2017**, *117*, 11302–11336. [[CrossRef](#)]
59. Zhong, L.; Brancho, J.J.; Batterman, S.; Bartlett, B.M.; Godwin, C. Experimental and modeling study of visible light responsive photocatalytic oxidation (PCO) materials for toluene degradation. *Appl. Catal. B Environ.* **2017**, *216*, 122–132. [[CrossRef](#)]



60. Mamaghani, A.H.; Haghghat, F.; Lee, C.-S. Photocatalytic oxidation technology for indoor environment air purification: The state-of-the-art. *Appl. Catal. B Environ.* **2017**, *203*, 247–269. [[CrossRef](#)]
61. He, F.; Muliane, U.; Weon, S.; Choi, W. Substrate-specific mineralization and deactivation behaviors of TiO<sub>2</sub> as an air-cleaning photocatalyst. *Appl. Catal. B Environ.* **2020**, *275*, 119145. [[CrossRef](#)]
62. Zou, W.; Gao, B.; Ok, Y.S.; Dong, L. Integrated adsorption and photocatalytic degradation of volatile organic compounds (VOCs) using carbon-based nanocomposites: A critical review. *Chemosphere* **2019**, *218*, 845–859. [[CrossRef](#)] [[PubMed](#)]
63. Chung, C.-J.; Lin, H.-I.; Chou, C.-M.; Hsieh, P.-Y.; Hsiao, C.-H.; Shi, Z.-Y.; He, J.-L. Inactivation of *Staphylococcus aureus* and *Escherichia coli* under various light sources on photocatalytic titanium dioxide thin film. *Surf. Coat. Technol.* **2009**, *203*, 1081–1085. [[CrossRef](#)]
64. Javid, A.; Kumar, M.; Ashraf, M.; Lee, J.H.; Han, J.G. Photocatalytic antibacterial study of N-doped TiO<sub>2</sub> thin films synthesized by ICP assisted plasma sputtering method. *Phys. E Low-Dimens. Syst. Nanostruct.* **2019**, *106*, 187–193. [[CrossRef](#)]
65. Li, Q.; Page, M.A.; Mariñas, B.J.; Shang, J.K. Treatment of Coliphage MS2 with Palladium-Modified Nitrogen-Doped Titanium Oxide Photocatalyst Illuminated by Visible Light. *Environ. Sci. Technol.* **2008**, *42*, 6148–6153. [[CrossRef](#)] [[PubMed](#)]
66. Thunyasirirong, C. Enhancement of Air Filter with TiO<sub>2</sub> Photocatalysis for Mycobacterium Tuberculosis Removal. *Aerosol Air Qual. Res.* **2015**, *15*, 600–610. [[CrossRef](#)]